Nano Research

Open Access

Research Article

Intermediate stabilization enables antisolvent-free crystallization of perovskites for high-performance light-emitting diodes

Wenjing Feng[1,§], Xi Chen[2,§], Yuhang Cui[1,§], Jiawei Chen[1], Enlong Hou[2], Jian Xu[3] ✉, Zhanhua Wei[2] ✉, and Dongxin Ma[1,4] ✉

[1] *Key Lab of Organic Optoelectronics and Molecular Engineering of Ministry of Education, Department of Chemistry, Tsinghua University, Beijing 100084, China*
[2] *Xiamen Key Laboratory of Optoelectronic Materials and Advanced Manufacturing, Institute of Luminescent Materials and Information Displays, College of Materials Science and Engineering, Huaqiao University, Xiamen 361021, China*
[3] *School of Interdisciplinary Science, Beijing Institute of Technology, Beijing 100081, China*
[4] *State Key Laboratory of Flexible Electronics Technology, Tsinghua University, Beijing 100084, China*
§ *Wenjing Feng, Xi Chen, and Yuhang Cui contributed equally to this work.*

Cite this article: *Nano Research*, **2026**, *19*, 94908503. https://doi.org/10.26599/NR.2026.94908503

ABSTRACT: Perovskites with superior optoelectronic properties are admirable candidates for high-performance light-emitting diode (LED) applications. However, the use of antisolvents during perovskite film fabrication increases process complexity and production costs, as well as raises toxicity concerns. Here, we demonstrated an antisolvent-free crystallization strategy enabled by intermediate stabilization for the fabrication of high-quality perovskite films. We prepared the reduced-dimensional perovskite precursor, and used cesium bromide as the crystallization retardant to facilitate the formation of stable intermediate during spin coating. This intermediate directs more ordered crystal growth and achieves a uniform quantum well thickness distribution, thereby substantially enhancing film quality. By using this approach, we fabricated LEDs with a maximum external quantum efficiency of 29.36%. This work elucidates the crystallization mechanism of perovskites and establishes an antisolvent-free pathway for the scalable and sustainable fabrication of high-performance perovskite optoelectronic devices.

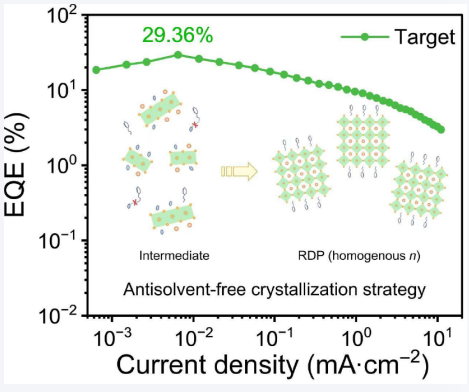

KEYWORDS: reduced-dimensional perovskites, light-emitting diodes, crystallization, intermediate stabilization

1 Introduction

Metal halide perovskites possess tunable optical bandgaps, narrow emission spectra, high photoluminescence quantum yields (PLQYs), and good charge mobility, making them attractive for a range of optoelectronic applications, including solar cells, lasers, photodetectors and light-emitting diodes (LEDs) [1–4]. Perovskite films for LEDs are typically fabricated via spin-coating, where precursors are dissolved in solvents such as dimethyl sulfoxide (DMSO) or N,N-dimethylformamide (DMF), then dripped on the substrate and spin-coated [5, 6]. During spin-coating, antisolvents are always introduced to promote rapid solvent volatilization and trigger crystallization, a strategy that has enabled high-performance perovskite LEDs [7–10]. However, antisolvent-assisted crystallization presents several limitations: (i) The rapid crystallization would lead to randomly oriented perovskite layers, non-uniform quantum well thickness distributions, and high defect densities, all of which are detrimental to the device performance; (ii) the narrow time window for antisolvent dripping would reduce process reproducibility and hamper large-area fabrication; (iii) the widely used antisolvents like toluene, chloroform and diethyl ether are toxic and environmentally unfriendly, posing challenges for scalable and sustainable manufacturing.

To tackle this issue, researchers sought to develop antisolvent-free strategies for perovskite film fabrication [11, 12]. These strategies could fundamentally circumvent the narrow processing time window and toxicity issues brought by antisolvent-assisted ones, while the key challenge lies in the imbalance between

Received: October 23, 2025; **Revised:** January 5, 2026
Accepted: January 29, 2026

✉Address correspondence to Jian Xu, jianxu.xu@bit.edu.cn; Zhanhua Wei, weizhanhua@hqu.edu.cn; Dongxin Ma, dongxinma@tsinghua.edu.cn

nucleation and crystal growth dynamics. In general, accelerating nucleation and delaying crystal growth are prerequisites for obtaining high-quality perovskite films, however, the antisolvent-free film-formation process undergoes slow nucleation and rapid crystal growth, inducing structural defects that would compromise the film quality of perovskites [13–15]. A potential solution is to stabilize the intermediate species and retard the growth kinetics, in order to improve film morphology and promise high-performance LEDs.

In this work, we propose an intermediate stabilization strategy to achieve antisolvent-free fabrication of high-quality perovskite films. By introducing extra cesium bromide (CsBr) as a crystallization retardant, we stabilize the intermediate during spin-coating, enabling the formation of perovskite films with monodispersed quantum well thickness, high PLQYs, narrow emission spectra, and good stability. By using this approach, we achieve LEDs with a maximum external quantum efficiency (EQE) of 29.36%, thereby offering a low-toxicity and eco-friendly route toward perovskite LED industrialization.

2 Results and discussion

2.1 Film fabrication and characterization

We focused on bromide-based reduced-dimensional perovskites (RDPs), and prepared the perovskite precursor solution by mixing lead bromide ($PbBr_2$, 0.30 mol·L^{-1}), phenylethylammonium bromide (PEABr, 0.12 mol·L^{-1}) and formamidinium bromide (FABr, 0.10 mol·L^{-1}) into DMSO, then added [2-(9H-carbazol-9-yl)ethyl]phosphonic acid (2PACz, 0.50 mg·mL^{-1}) as the molecular dopant [16] and CsBr as the crystallization retardant (ranging from 0.24 to 0.54 mol·L^{-1}). When more CsBr was added, the precursor solution became a supersaturated state with white precipitate (Fig. S1(a) in the Electronic Supplmentary Material (ESM)). We then fabricated thin films based on the filtered precursor solutions, and no antisolvent was used throughout the entire process (see Experimental Section). We observed that the thin films before annealing gradually transitioned from light green to colorless transparent with the addition of CsBr (Fig. S1(a) in the ESM), along with a gradient reduction in photoluminescence (PL) intensity (Fig. S1(b) in the ESM). Remarkably, the PL emission became negligible when 0.48 mol·L^{-1} or more CsBr was added, probably due to the formation of stable intermediates in the thin film, which slowed down the crystallization of perovskite and reduced the luminescence. Thus, we chose the precursor solution with the addition of 0.48 mol·L^{-1} CsBr to fabricate the target perovskite thin film for the following investigation, compared to the control one with 0.24 mol·L^{-1} CsBr.

We found that, under UV excitation, the control films showed green emission before and after annealing, and the latter was brighter; while the target films showed no emission until annealing (Fig. 1(a)). We first investigated the optical properties of the perovskite films before and after annealing (labeled as raw and

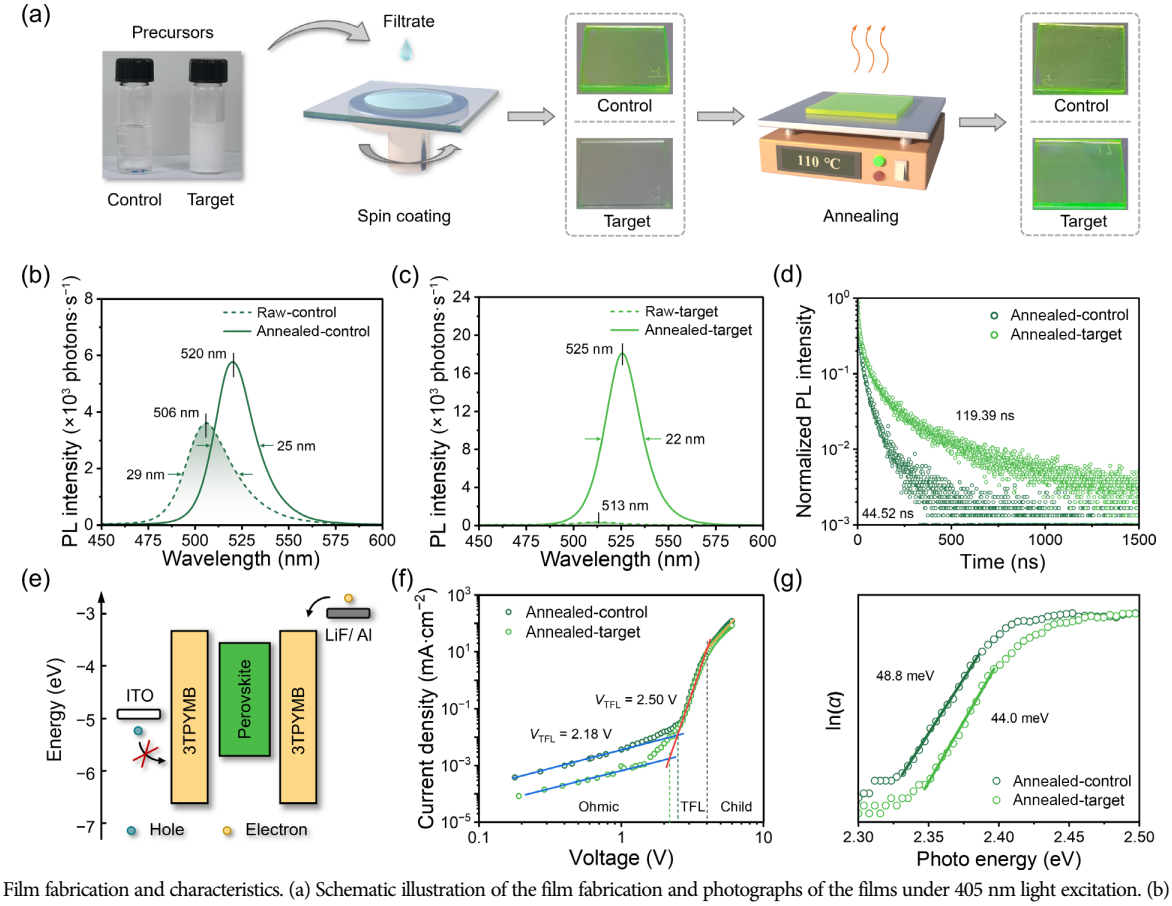

Figure 1 Film fabrication and characteristics. (a) Schematic illustration of the film fabrication and photographs of the films under 405 nm light excitation. (b) and (c) PL spectra of the raw and annealed films. (d) TRPL spectra of the annealed films. Here the time-correlated single photon counting (TCSPC) was employed with a pulsed excitation at 375 nm. (e) The energy-level diagram of the electron-only devices. (f) Current density–voltage curves of the electron-only devices. (g) Absorption coefficient as a function of photon energy of the annealed films.

annealed control or target films, respectively). The raw control film showed PL spectra peaked at 506 nm with a full width at half maximum (FWHM) of 29 nm, and the emission of the annealed control film red-shifted to 520 nm, with enhanced intensity, PLQY of 64% and FWHM of 25 nm (Fig. 1(b)), indicating that the annealing process enhanced the crystal quality and narrowed the quantum well thickness distribution of the control film. In comparison, the raw target film was nearly colorless and showed quite weak emission, with the peak centering at approximately 513 nm, suggesting the existence of intermediate and delayed crystallization. However, the annealed target film showed very high PL intensity, and the PL peak was located at 525 nm with near-unity PLQY and a smaller FWHM of 22 nm (Fig. 1(c)).

The ultraviolet–visible (UV–vis) absorption spectra showed that the absorption band edge of the raw control films was located at 515 nm, while red-shifted to 530 nm after annealing (Fig. S2(a) in the ESM), suggesting that the raw control film was in a semi-crystalline state, and the annealing process facilitated the growth and complete transformation of perovskites. However, the target films exhibited extremely distinguishing absorption characteristics before and after annealing (Fig. S2(b) in the ESM). The absorption curve of the raw target film with an absorption band edge at 373 nm was mostly attributed to the characteristic absorption peak of the intermediate species, indicating that there were no perovskites formed in the raw target film. In contrast, the annealed target film with an absorption band edge of 527 nm showed a significant absorption characteristic of perovskites.

We then used X-ray diffraction (XRD) to investigate the microstructure of these films. The diffraction peaks at 15.07° were attributed to the bulk $CsPbBr_3$, corresponding to (100) crystal planes (Figs. S3(a) and S3(b) in the ESM) [17]. Other diffraction peaks near 16.59°, 25.95°, and 30.34° belonged to the RDP quantum wells with different n values, and the attribution of each diffraction peak was marked [18]. In the raw control films, there were both diffraction peaks of RDP and $CsPbBr_3$ phases, indicating the co-existence of 2D/3D hybrid perovskites (Fig. S3(a) in the ESM). By contrast, in the raw target films, there were only RDP phases, providing evidence that the extra CsBr could delay the crystallization process and facilitate the formation of intermediate species. After annealing, the diffraction peak of RDP quantum well of n = 1 at 25.95° disappeared, and the diffraction peak of $CsPbBr_3$ appeared in both the annealed films (Figs. S3(b) and S3(c) in the ESM), indicating that the annealing process accelerated the phase transformation. The ratios of diffraction peak areas between $CsPbBr_3$ at 30.19° and RDP quantum wells at 30.53° were 1.28 and 6.25 for the annealed control and target films (Fig. S3(d) in the ESM), respectively, indicating that, compared with the control one, the RDP quantum wells with smaller n values were suppressed in the annealed target films. The above results indicated that, under the control condition, the perovskite crystallization was accelerated, facilitating the formation of RDP quantum wells with a mixed n-value distribution. However, the presence of extra CsBr delayed the perovskite crystallization process, suppressed the formation of quantum wells with low n-values, and ultimately formed the RDP quantum wells with a homogeneous n-value distribution. Scanning electron microscopy (SEM) characteristics also supported the conclusion. The surface morphology of the raw control and target film was similar (Figs. S4(a) and S4(b) in the ESM), while the annealed target film exhibited distinguishing surface morphology compared with the annealed control one (Figs. S4(c) and S4(d) in the ESM). Atomic force microscope (AFM) images revealed that the annealed target film possessed a higher root mean square (RMS) roughness of 2.86 nm than 1.59 nm for the annealed control film (Fig. S5 in the ESM). The phenomena suggested that extra CsBr could facilitate the formation of the intermediate and slow down the perovskite crystallization, causing the discrepancy of resultant thin films in the microstructure and surface morphology.

We further evaluated the quality of RDP thin films with mixed and homogeneous n-value quantum wells distributions by using PL stability, time-resolved photoluminescence (TRPL) spectra, and Urbach energy (E_U) measurements. The annealed control film showed decreased emission intensity and PLQY after three hours of continuous excitation, while the annealed target one showed stable PL and PLQY (Figs. S6 and S7 in the ESM), which was probably ascribed to the increased exciton binding energy (E_b) and reduced defect density.

We conducted temperature-dependent PL measurements to quantitatively extract the E_b. For both the annealed control and target films, the PL intensity reduced and the PL peak blue-shifted along with the increasing temperature, owing to the enhanced electron-phonon coupling and thermally activated non-radiative losses (Figs. S8(a) and S8(b) in the ESM) [19]. The annealed control film presented multiple PL peaks at low temperatures, suggesting the impure species; while the annealed target one primarily exhibited a single peak at around 523 nm. The extracted E_b values were estimated to be 50.3 and 80.0 meV for the annealed control and target films (Figs. S8(c) and S8(d) in the ESM), respectively. This elevated E_b in the latter might originate from the fact that the reduction of defect states mitigated nonradiative recombination, consistent with the PLQY results.

Moreover, TRPL spectra indicated that the annealed target film showed a transient longer lifetime than the control one did, due to the reduced defect density and increased bimolecular radiation recombination (Fig. 1(d) and Table S1 in the ESM). We then fabricated electron-only devices with a structure of indium tin oxide (ITO)/tris[2,4,6-trimethyl-3-(pyridin-3-yl)phenyl]borane (3TPYMB)/perovskite/3TPYMB/lithium fluoride (LiF)/aluminium (Al) to estimate the defect density of the annealed control and target films (Fig. 1(e)). According to the current density curves in Fig. 1(f), the trap-filled limit voltages (V_{TFL}) of the annealed control and target films were 2.50 and 2.18 V, respectively. According to the equation [20]: $N_{defects} = 2\varepsilon\varepsilon_0 V_{TFL}/eL^2$, the corresponding electronic defect densities ($N_{defects}$) were calculated to be 2.58×10^{18} and 2.25×10^{18} cm^{-3} for the annealed control and target films, respectively. E_U was extracted from the optical absorption measurements to evaluate the energetic disorder of the films (Fig. 1(g) in the ESM), and the E_U values of the annealed control and target ones were 48.8 and 44.0 meV, respectively, indicative of lower band edge energy disorder and defect density for the latter [21].

2.2 Mechanism of perovskite crystallization

Inspired by the above results, we sought to study the mechanism of perovskite crystallization, including intermediate formation and transformation.

To investigate the mechanism of intermediate formation, we began with the filtered perovskite precursor solutions. Under UV lamp, both the control and target solutions showed weak yellow emission peaked at 564 nm (Fig. S9(a) in the ESM), which was derived from the $[PbBr_4{\cdot}2DMSO]^{2-}$ complex [22]. The increased Br^- concentration from extra CsBr facilitated the formation of a more

stable and increased population of $[PbBr_4{\cdot}2DMSO]^{2-}$ complex in the target supernatant. Compared with the control one, the PL intensity of the target precursor solution markedly decreased (Fig. S9(b) in the ESM), mostly due to the solvent effect quenching triggered by the strong interaction between solvent and fluorescent substances at a higher concentration of the $[PbBr_4{\cdot}2DMSO]^{2-}$ complex. UV–vis absorption spectra of both the control and target precursor solutions showed the same absorption plateau edge at 378 nm (Fig. S9(c) in the ESM), and the target solution exhibited slightly higher absorption intensity than the control one did, also indicative of a higher concentration of $[PbBr_4{\cdot}2DMSO]^{2-}$ complex in the former. Moreover, extra Cs^+ reduced the colloidal size and enhanced colloidal stability, owing to its strong binding affinity with $[PbBr_4{\cdot}2DMSO]^{2-}$, which suppressed ion exchange between Cs^+ and PEA^+ during nucleation and crystal growth. Dynamic light scattering (DLS) spectra showed a much narrower size distribution in the target solution compared to the control one (Fig. S9(d) in the ESM), consistent with the role of extra CsBr in reducing colloidal particle size. The presence of smaller colloidal particles increases the Gibbs free energy barrier during nucleation and crystal growth, thereby delaying perovskite crystallization.

We then used these precursor solutions to fabricate thin films, and set up an *in-situ* PL test equipment based on the real film-formation environment to monitor the perovskite crystallization process and investigate the nucleation kinetics. A 375 nm laser diode coupled with a visible-range spectrometer was used to track the *in-situ* PL emission during spin coating and thermal annealing (Fig. S10 in the ESM). We observed clear differences in PL intensity and peak positions between the control and target films (Figs. 2(a)–2(d)). Correspondingly, the components also continuously changed in the control and target films during spin coating and thermal annealing (Fig. 2(e)).

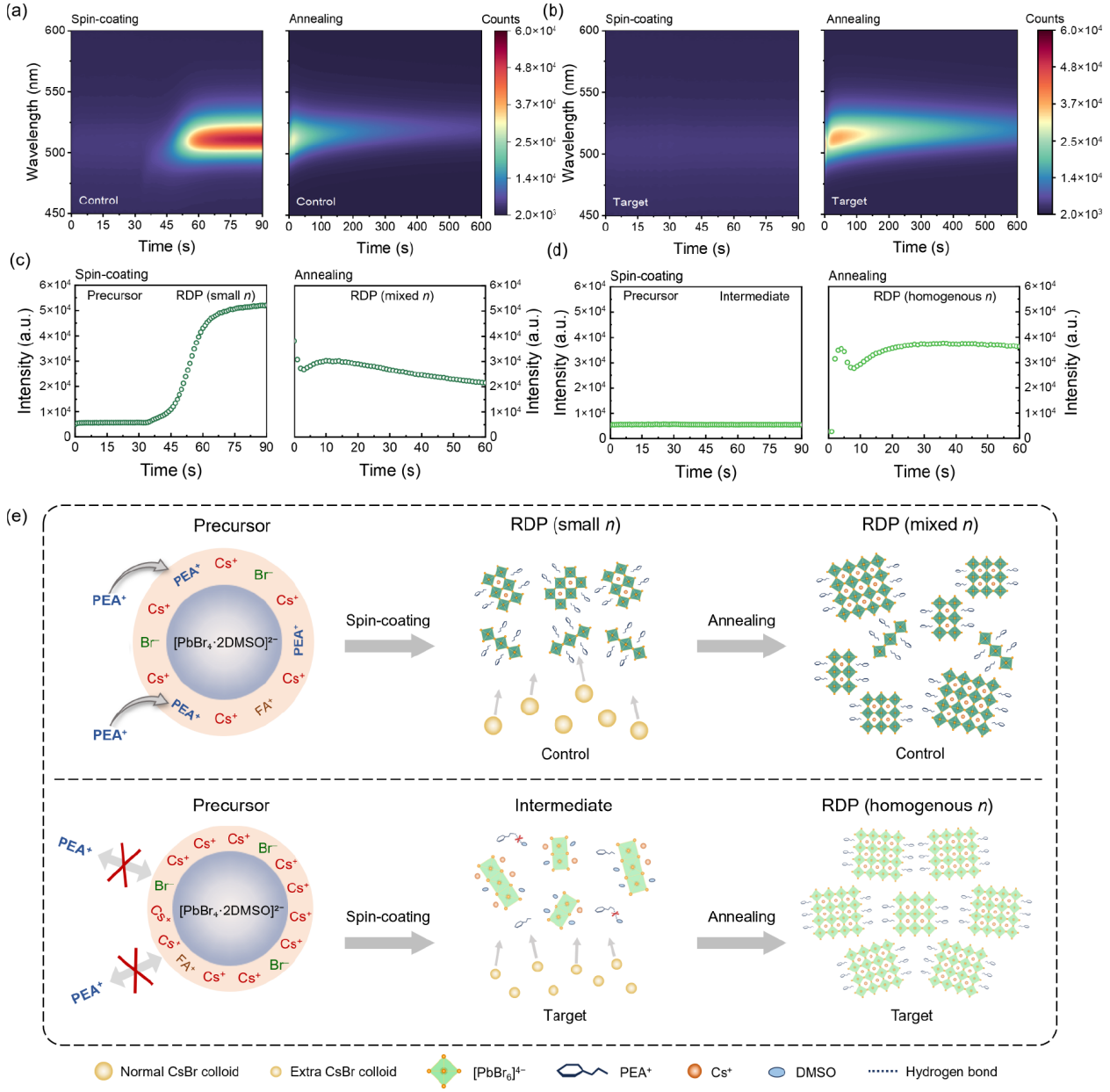

Figure 2 Perovskite crystallization process analysis. (a) and (b) *In-situ* PL spectra and ((c) and (d)) PL intensity of the control and target films during spin coating and annealing, respectively. (e) Schematic illustration of the intermediate formation and transformation process for the control and target films.

At the initial stage of spin coating, the precursor monomer, i.e., $[PbBr_4{\cdot}2DMSO]^{2-}$ complexes, PEABr, and CsBr of free state, dominated. Subsequently, the continuous volatilization of DMSO promoted the perovskite precursor solution to reach a supersaturation state, leading to nucleation and subsequent growth. The control films showed light emission after approximately 35 s, the PL intensity tardily increased and reached the maximum value at the end, and the corresponding PL peak red-shifted from 495 to 510 nm, indicating the formation of RDP quantum wells with smaller *n* values (Figs. 2(a) and 2(c)). During thermal annealing, as the residual solvent sharply volatilized, the PL intensity sharply decreased in the first 3 s, probably because the fusion and growth of tiny grains promoted defect formation, which led to serious nonradiative recombination [23]. In the subsequent 7 s, i. e., 3–10 s, the PL intensity gradually enhanced due to the secondary growth of the perovskite grains; and began to decrease after 10 s. The latter could be ascribed to that the continuous annealing not only promoted the formation of thermally activated carrier traps within the perovskites, which increased the nonradiative recombination; but also caused lattice vibration of the perovskites, which reduced the excitation energy of the luminescence center [24]. At this stage, crystallization of the perovskite was finished, with the formation of the RDP quantum wells with mixed *n* values (Fig. 2(e)).

By contrast, during spin coating, the target film showed quite weak emission due to the formation of intermediate species, i. e., $CsBr{\cdot}PbBr_2{\cdot}DMSO$ complex [25]. However, during the first 4 s of thermal annealing, these intermediate species underwent dissociation followed by transformation into perovskites, so the PL intensity sharply increased to the maximum (Figs. 2(c) and 2(d)), indicating a delayed but much faster perovskite crystallization. Afterward, the PL intensity showed a similar evolution to that of the control film did, but the RDP quantum wells with homogenous *n* values were formed (Fig. 2(e)). The PL intensity decreased in the subsequent 4 s, then enhanced during 8–36 s, with a much longer period compared with the control film, suggesting slower grain growth. After 36 s, the PL peak intensity slowly decreased, indicative of a better thermal stability of the target film.

In addition, the PL peak of the control and target films also exhibited great differences. For the control film, the PL peak started at 495 nm during spin coating, and continuously red-shifted to 520 nm at the end of thermal annealing. For the target film, the PL peak blue-shifted from 513 to 506 nm during the first 6 s of thermal annealing, which was attributed to the stronger quantum confinement caused by the RDP phases; then gradually red-shifted to 519 nm at the end.

The above phenomena demonstrated that extra CsBr in the raw target film would facilitate the formation of intermediate, stabilize the intermediate, and slow down the perovskite crystallization; and the following thermal annealing promoted the transformation of intermediate towards the RDP quantum wells with homogenous *n* values.

We then turned to investigate the intermediate in the raw target film. As is known, DMSO could serve as a Lewis base and covalently bond to $PbBr_2$ to form $[PbBr_4{\cdot}2DMSO]^{2-}$ complex, while extra CsBr was also prone to strongly ionically bond to $[PbBr_4{\cdot}2DMSO]^{2-}$. Hence, the coexistence of two interacting forces would promote the formation and stability of $CsBr{\cdot}PbBr_2{\cdot}DMSO$ complex in the target film during spin-coating. We used ^{1}H nuclear magnetic resonance (^{1}H-NMR) to verify the existence of the $CsBr{\cdot}PbBr_2{\cdot}DMSO$ complex in the raw target film. We dissolved the raw and annealed control and target films, respectively, into deuterated DMSO to quantify the residual solvent, DMSO. We observed the obvious DMSO signal peaked at 2.54 ppm in the raw films (Fig. S11 in the ESM). The existence form of DMSO could be interpreted through a dual pathway mechanism: a fraction of DMSO solvent molecules were retained within the raw film matrix as residual species that did not participate in the reaction with perovskite precursor, while concurrently, another population of DMSO molecules underwent chemical interactions with the precursor species, thereby facilitating the formation of $CsBr{\cdot}PbBr_2{\cdot}DMSO$ complex that would serve as stable intermediates during crystallization. However, the peak area of DMSO in the raw target film was larger than that of DMSO in the control one (Fig. S11(a) in the ESM), indicating that there were more $CsBr{\cdot}PbBr_2{\cdot}DMSO$ complexes in the former. Meanwhile, we also analyzed the DMSO signal in the annealed films (Fig. S11(b) in the ESM). Compared with the raw films, the peak signal of DMSO in annealed films was negligible, indicating that annealing would not only accelerate the volatilization of the DMSO solvent, but also destroy the chemical interactions between DMSO and the precursor species, then promote the transformation of intermediates towards perovskites.

To further understand the mechanism of perovskite crystallization, we conducted ab-initio molecular dynamics (AIMD) simulations on the control and target precursor solutions, mirroring the experimental conditions. Specifically, we constructed models for the control and target precursor solutions. In both models, ions and molecules were initially distributed evenly, and AIMD simulations were carried out for 14 ps in the constant-pressure and -temperature (NPT) ensemble, followed by 10 ps in the constant-volume and -temperature (NVT) ensemble. The temperature was maintained at 300 K, and the pressure was set at 1 bar (atmospheric pressure). After reaching equilibrium, we observed substantial differences between the two models (Figs. 3(a) and 3(b), and Videos S1 and S2 in the ESM). In the control model, 50% of the DMSO molecules bound with Cs^+, while no binding occurred between DMSO and $PbBr_2$. By contrast, in the target model, 75% of the DMSO molecules bound with Cs^+, and a strong interaction between DMSO and $PbBr_2$ was observed, supporting the formation of a more stable intermediate species, specifically the $CsBr{\cdot}PbBr_2{\cdot}DMSO$ complex. Our AIMD simulations thus corroborated the experimental evidence and confirmed that the introduction of extra CsBr into the precursor solution would facilitate the formation of intermediate complexes, which played a crucial role in stabilizing the crystallization process.

2.3 LED performance

We then fabricated LEDs with a device structure of ITO/nickel oxide (NiO_x, 5 nm)/self-assembled monolayer (SAM, ~ 1 nm)/poly(9-vinylcarbazole) (PVK, 10 nm)/perovskite (45 nm)/3TPYMB (40 nm)/LiF (1 nm)/Al (100 nm), as shown in Figs. 4(a)–4(c). Herein, we focused on the electrical analysis of LEDs based on the annealed control and target films (labeled as control and target device, respectively). The control and target devices showed similar electroluminescence (EL) spectra peaked at 523 and 521 nm (Fig. 4(d)), corresponding to the Commission Internationale de l'Eclairage color-space coordinates of (0.13, 0.78) and (0.11, 0.78), respectively (Fig. 4(e)). Compared to the control one, the target device showed higher current density, indicating that the extra CsBr

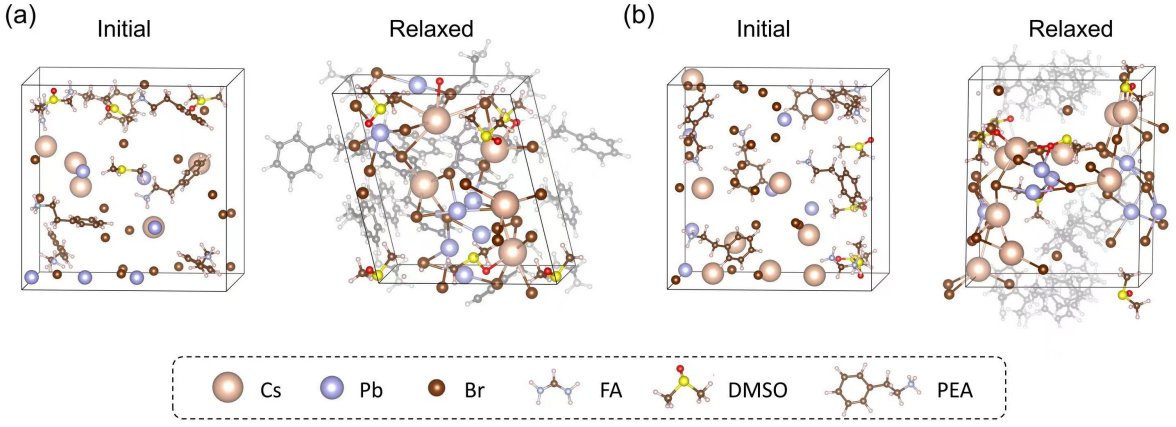

Figure 3 Molecular dynamics simulations. (a) Initial and relaxed configurations of the control precursor solution model, obtained from AIMD simulations. (b) Initial and relaxed configurations of the target precursor solution model, obtained from AIMD simulations. In the relaxed configurations, for clarity, only DMSO molecules, Pb^{2+}, Cs^{+}, and Br are highlighted, while all other ions and solvent molecules are rendered transparent.

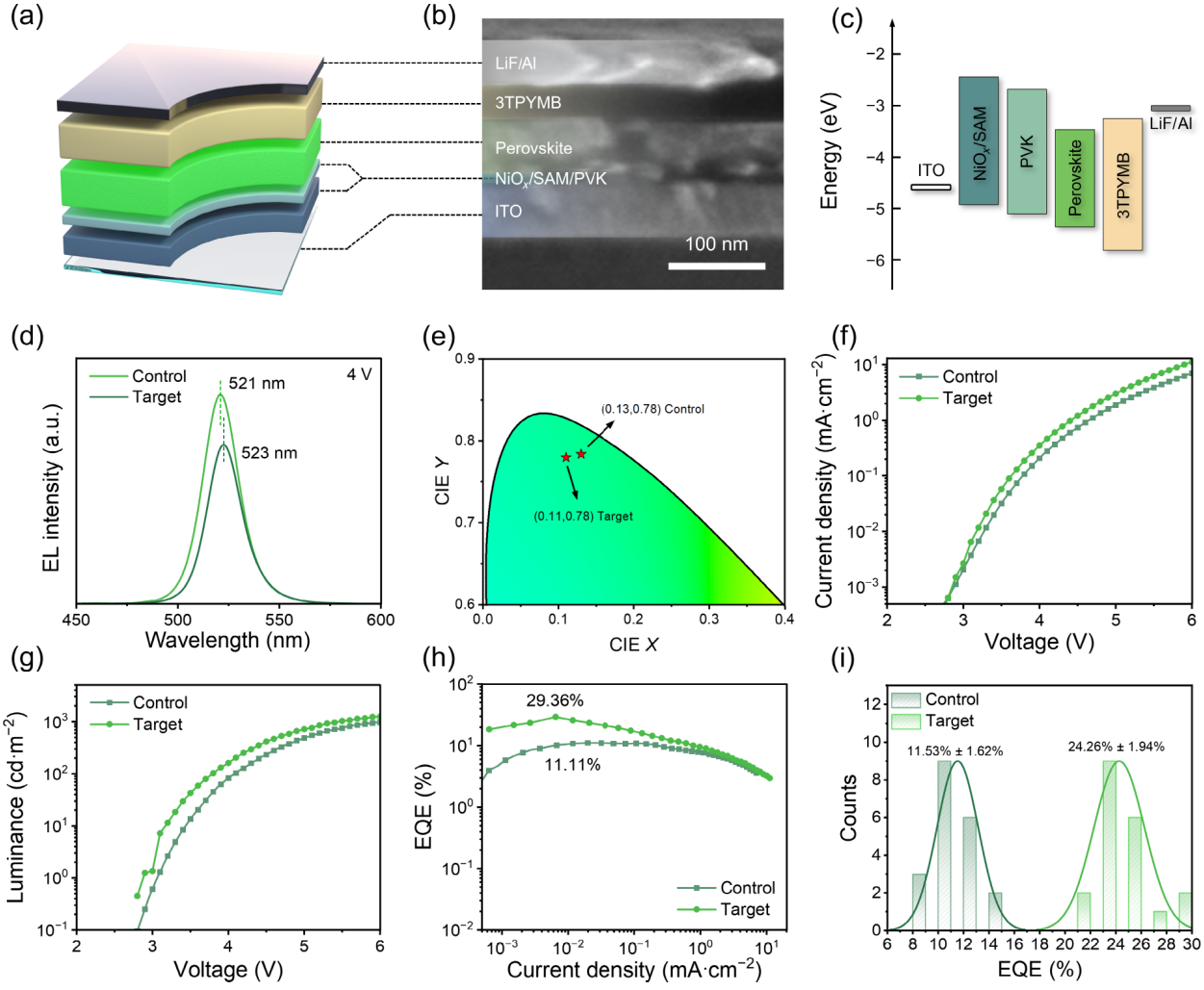

Figure 4 Device performance. (a) Schematic diagram of the device structure, (b) cross-sectional SEM image, (c) energy band diagram, (d) EL spectra, (e) CIE chromatic diagram, (f) current density–voltage curves, (g) luminescence–voltage curves, and (h) EQE–current density curves of the control and target LEDs. (i) The EQE statistics histogram of the control and target LEDs.

could enhance the charge transport due to the suppressed quantum wells with small *n* (Fig. 4(f)). The lower turn-on voltage of only 2.8 V and higher luminance (Fig. 4(g)) could be predominantly attributed to the increscent bimolecular radiative recombination rate at low current density, which thereby improved the radiative efficiency. As a result, the target devices achieved a maximum EQE of 29.36% (Figs. 4(h) and 4(i)), and an operating half-life of 411 min (6.85 h) at an initial luminance of 300 cd·m^{-2} (Fig. S12 in the ESM).

3 Conclusion

In summary, we demonstrated that extra CsBr in RDP precursors could stabilize the intermediate, slow down the perovskite crystallization process, thereby contributing to more ordered crystal growth and uniform quantum well thickness distribution. This intermediate stabilization strategy enabled us to fabricate high-quality RDP films without using antisolvents during the entire film processing, achieving monodispersed quantum wells, high PLQY, small FWHM, and good stability. We then constructed perovskite LEDs with a maximum EQE of 29.36% and an operating half-life of 411 min (6.85 h) at an initial luminance of 300 cd·m^{-2}. Our work elucidates the underlying crystallization dynamics of antisolvent-free perovskite fabrication and establishes an eco-friendly production strategy for commercially viable perovskite LEDs.

4 Experimental section

4.1 Materials

CsBr (99.999%), $PbBr_2$ (99.999%), ethanol (99.8%), chlorobenzene (anhydrous, 99.8%), and LiF were purchased from Sigma-Aldrich. PEABr (99.5%) and FABr (> 99.99%) were purchased from Greatcell Solar Materials. DMSO (> 99.0%) was purchased from Acros Organics. NiO_x (99.999%) was purchased from Liaoning Advanced Election Technology Co., Ltd. 2PACz (> 98.0%) and [4-(7H-dibenzo[c,g]carbazol-7-yl)butyl]phosphonic acid (4PADCB) were purchased from TCI. PVK (number-average molecular weight > 100,000 g·mol^{-1}) and 3TPYMB were purchased from Lumtec. All chemicals were used as received without further purification.

4.2 Solution preparation

For the NiO_x precursor solution, NiO_x nanocrystals were dissolved in H_2O at a concentration of 5 mg·mL^{-1}. For the SAM solution, 4PADCB was dissolved in ethanol at a concentration of 1 mg·mL^{-1}. For the PVK solution, PVK was dissolved in chlorobenzene at a concentration of 6 mg·mL^{-1}. All solutions were continuously stirred for 12 h at room temperature.

4.3 Device fabrication

Prepatterned ITO conductive glasses (20 mm × 20 mm, 20 Ω, Advanced Election Technology) were first cleaned with detergent. Then the substrates were sonicated in deionized water, acetone, isopropanol, and ethanol for 20 min in sequence. After drying with compressed nitrogen flow, the substrates were treated with oxygen plasma for 10 min. The NiO_x solution was filtered, and spin-coated onto the ITO substrates at 4000 r.p.m. for 20 s in ambient air, and the resulting films were annealed at 150 °C for 10 min, and transferred to the nitrogen-filled glovebox. The SAM solution was spin-coated (2000 r.p.m. for 30 s) onto the ITO/NiO_x-coated substrates, and the resulting films were annealed at 100 °C for 10 min, cooled down to room temperature, washed with ethanol (3000 r.p.m. for 50 s), and again annealed at 100 °C for 10 min. The PVK solution was spin-coated at 2000 r.p.m. for 30 s, and the films were then annealed at 150 °C for 30 min. The perovskite precursor solutions were spin-coated at 4000 r.p.m. for 90 s, and the films were then annealed at 110 °C for 10 min. Then, the ITO/NiO_x/SAM/PVK/perovskite-coated substrates were transferred into a thermal evaporator to prepare the electron transporter layer and cathode. The chamber was vacuum-pumped down to 5.0×10^{-4} Pa, and 3TPYMB (40 nm), LiF (1 nm) and Al (100 nm) were sequentially evaporated at the rate of 1.5, 0.1, and 2.0 Å·s^{-1}, respectively. The device area (1.5 mm × 2 mm, 3 mm^2) was defined by the overlap of Al and ITO.

4.4 Characterization

SEM images were recorded by using a field-emission SEM (JSM-7610F Plus, JEOL). Cross-sectional SEM samples were prepared by mechanical cutting of the device using a diamond cutter. UV–vis absorption, steady-state PL spectra, and PLQY data were measured using a QE-Pro spectrometer (Ocean Optics). TRPL spectra were measured by using the FLS1000 (Edinburgh Instruments, Ltd.) with a pulsed excitation at 375 nm. The PL decay curves were fitted by applying the triple-exponential equation

$$I = A_1 \exp\left(-\frac{t}{\tau_1}\right) + A_2 \exp\left(-\frac{t}{\tau_2}\right) + A_3 \exp\left(-\frac{t}{\tau_3}\right) \quad (1)$$

And the average lifetimes were calculated following the formula below

$$\tau_{avg} = \frac{A_1\tau_1^2 + A_2\tau_2^2 + A_3\tau_3^2}{A_1\tau_1 + A_2\tau_2 + A_3\tau_3} \quad (2)$$

XRD patterns were recorded on a Smartlab diffractometer (Rigaku, Japan). *In-situ* PL spectra were measured by using a home-built platform. A 375 nm laser diode was used as an excitation source, and PL emission was collected by using a visible-range spectrometer (Ocean Optics) connecting an optical fiber. The laser diode and optical fiber were fixed, and the intensity of light source remained unchanged throughout the whole testing process. The ^{1}H NMR spectra were acquired by using a Bruker 500 MHz AVANACIII NMR spectrometer (Bruker Biospin). The characterization techniques mentioned above were all conducted in the nitrogen atmosphere. UV–vis absorption spectra of perovskite precursor solutions were measured by using a U-3900H spectrophotometer (HITACHI). Steady-state PL spectra of perovskite precursor solutions were recorded by using an F-7000 Fluorescence spectrophotometer (HITACHI). The colloid size distribution was studied by DLS (NanoBrook Omni). All of the devices were measured in the nitrogen-filled glovebox, by using a source meter (Keithley 2400) and a commercialized system (XPQY-EQE, Guangzhou Xi Pu Optoelectronics Technology Co., Ltd.) that was equipped with an integrated sphere (GPS-4P-SL, Labsphere) and a QE-Pro spectrometer (Ocean Optics). Before each measurement, careful calibration (HL-3 Radiometric calibrated light source, Ocean Optics) and sample holder selection were conducted for the XPQY-EQE.

4.5 Computational details

AIMD simulations were conducted by using the CP2K package [26]. We constructed the model for the control perovskite precursor solution with a mixture of ions and molecules: 6 Pb^{2+}, 18 Br^-, 5 Cs^+, 1 FA^+, 4 DMSO and 6 PEA^+, while the model for the target perovskite precursor solution with a mixture of ions and molecules: 6 Pb^{2+}, 22 Br^-, 9 Cs^+, 1 FA^+, 4 DMSO and 6 PEA^+. In both models, all ions and molecules were evenly distributed in the initial configuration, which was generated using Packmol software [27]. The AIMD simulations were run for 14 ps in the NPT ensemble, followed by 10 ps in the (NVT ensemble. The temperature was

controlled by using the Nosé–Hoover thermostat [28] at 300 K. The pressure was set to 1 bar (atmospheric pressure), and the time step was set to 1.0 fs. PBE-D3 functional was used with double-zeta basis sets (DZVP-MOLOPT) [29] and Goedecker–Teter–Hutter (GTH) pseudopotentials [30]. The cut-off was set to 560 Ry.

Electronic Supplementary Material: Supplementary material (PL, UV–vis absorption spectra, XRD, SEM, AFM, time-dependent PL spectra and PLQY, temperature-dependent PL, DLS spectra, ^{1}H NMR, operating lifetime of the device, and fitting data of the PL decay) is available in the online version of this article at https://doi.org/10.26599/NR.2026.94908503.

Data availability

All data needed to support the conclusions in the paper are presented in the manuscript and the Electronic Supplementary Material. Additional data related to this paper may be requested from the corresponding author upon request.

Acknowledgements

This work was financially supported by the National Natural Science Foundation of China (Nos. 52573201, 22509015, and 62504114), the Tsinghua University Initiative Scientific Research Program (Tsinghua University Dushi Program), the BIT Teli Young Fellow program, and the Fundamental Research Funds for the Central Universities (No. 30925020228).

Declaration of competing interest

All the contributing authors report no conflict of interests in this work.

Author contribution statement

D. X. M. and Z. H. W. conceived the idea and supervised the work. W. J. F., X. C., and Y. H. C. jointly completed the experiments, analyzed the data, and wrote the paper. J. X. carried out theoretical calculations and participated in the writing. J. W. C. helped to analyze the data. E. L. H. participated in the fabrication of the hole transport layer. All the authors have approved the final manuscript.

Use of AI statement

None.

References

[1] Yuan, L. G.; Xue, Q. F.; Wang, F.; Li, N.; Waterhouse, G. I. N.; Brabec, C. J.; Gao, F.; Yan, K. Y. Perovskite solar cells and light emitting diodes: Materials chemistry, device physics and relationship. *Chem. Rev.* **2025**, *125*, 5057–5162.

[2] Shi, Y.; Deng, X. Y.; Gan, Y. S.; Xu, L. B.; Zhang, Q.; Xiong, Q. H. Ten years of perovskite lasers. *Adv. Mater.* **2025**, *37*, 2413559.

[3] Yang, J.; Wang, W.; Bao, C. X.; Huang, W.; Wang, J. P. Toward practical applications of perovskite photodetectors: Advantages and challenges. *Matter* **2025**, *8*, 102207.

[4] Cheng, Y. Z.; Wan, H. Y.; Sargent, E. H.; Ma, D. X. Reduced-dimensional perovskites: Quantum well thickness distribution and optoelectronic properties. *Adv. Mater.* **2025**, *37*, 2410633.

[5] Wang, S. X.; Yu, Z. Q.; Qin, J. J.; Chen, G. Y.; Liu, Y. J.; Fan, S. W.; Ma, C.; Yao, F.; Cui, H. S.; Zhou, S. et al. Buried interface modification and light outcoupling strategy for efficient blue perovskite light-emitting diodes. *Sci. Bull.* **2024**, *69*, 2231–2240.

[6] Yu, H. Q.; Chen, W. J.; Fang, Z. B.; Ding, L. M.; Cao, B. Q.; Xiao, Z. G. Alkalis-doping of mixed tin-lead perovskites for efficient near-infrared light-emitting diodes. *Sci. Bull.* **2022**, *67*, 54–60.

[7] Lin, K. B.; Xing, J.; Quan, L. N.; De Arquer, F. P. G.; Gong, X. W.; Lu, J. X.; Xie, L. Q.; Zhao, W. J.; Zhang, D.; Yan, C. Z. et al. Perovskite light-emitting diodes with external quantum efficiency exceeding 20 per cent. *Nature* **2018**, *562*, 245–248.

[8] Ma, D. X.; Lin, K. B.; Dong, Y. T.; Choubisa, H.; Proppe, A. H.; Wu, D.; Wang, Y. K.; Chen, B.; Li, P. C.; Fan, J. Z. et al. Distribution control enables efficient reduced-dimensional perovskite LEDs. *Nature* **2021**, *599*, 594–598.

[9] Bai, W. H.; Xuan, T. T.; Zhao, H. Y.; Dong, H. R.; Cheng, X. R.; Wang, L.; Xie, R. J. Perovskite light-emitting diodes with an external quantum efficiency exceeding 30%. *Adv Mater* **2023**, *35*, 2302283.

[10] Kim, B. W.; Im, S. H. Supersaturated antisolvent-assisted crystallization for highly efficient inorganic perovskite light-emitting diodes. *ACS Nano* **2024**, *18*, 28691–28699.

[11] Xing, Z. H.; Jin, G. R.; Du, Q.; Pang, P. Y.; Liu, T. H.; Shen, Y.; Zhang, D. L.; Yu, B. F.; Liang, Y.; Yang, D. Z. et al. Ions-induced assembly of perovskite nanocomposites for highly efficient light-emitting diodes with EQE exceeding 30%. *Adv. Matter.* **2024**, *36*, 2406706.

[12] Jiang, M. W.; Li, L.; Qi, Z. W.; Wang, F. J. Efficient rec. 2020 Compliant pure-green mixed-cation perovskite light-emitting diodes with multifunctional co-additives. *Adv. Mater.* **2025**, *37*, 2503683.

[13] Kumar, J.; Srivastava, P.; Bag, M. Advanced strategies to tailor the nucleation and crystal growth in hybrid halide perovskite thin films. *Front. Chem.* **2022**, *10*, 842924.

[14] Xie, Y. M.; Xue, Q. F.; Yip, H. L. Metal-halide perovskite crystallization kinetics: A review of experimental and theoretical studies. *Adv. Energy Mater.* **2021**, *11*, 2100784.

[15] Peng, S.; Liu, Y. L.; Liu, Y.; Wang, H.; Ma, M. Y.; Zhou, W. J.; Xu, R. Q.; Jiang, X. Y.; Yu, D. N.; Zhou, W. et al. *In-situ* growth of titanium alkoxide network encapsulated perovskite nanograin for robust light emission. *Nano Res.* **2025**, *18*, 94907272.

[16] Xiong, W. T.; Tang, W. D.; Zhang, G.; Yang, Y. C.; Fan, Y. N.; Zhou, K.; Zou, C.; Zhao, B. D.; Di, D. W. Controllable p- and n-type behaviours in emissive perovskite semiconductors. *Nature* **2024**, *633*, 344–350.

[17] Feng, W. J.; Zhao, Y. P.; Lin, K. B.; Lu, J. X.; Liang, Y. M.; Liu, K. K.; Xie, L. Q.; Tian, C. B.; Lyu, T. S.; Wei, Z. H. Polymer-assisted crystal growth regulation and defect passivation for efficient perovskite light-emitting diodes. *Adv. Funct. Mater.* **2022**, *32*, 2203371.

[18] Jiang, Y. Z.; Cui, M. H.; Li, S. S.; Sun, C. J.; Huang, Y. M.; Wei, J. L.; Zhang, L.; Lv, M.; Qin, C. C.; Liu, Y. F. et al. Reducing the impact of Auger recombination in quasi-2D perovskite light-emitting diodes. *Nat. Commun.* **2021**, *12*, 336.

[19] Schmidt, T.; Lischka, K.; Zulehner, W. Excitation-power dependence of the near-band-edge photoluminescence of semiconductors. *Phys. Rev. B* **1992**, *45*, 8989–8994.

[20] Chen, J. W.; Chen, S. L.; Liu, X. Y.; Zhu, D. L.; Cai, B.; Luo, X. Y.; Feng, W. J.; Cheng, Y. Z.; Xiong, Y. N.; Du, J. Y. et al. Molecule-induced ripening control in perovskite quantum dots for efficient and stable light-emitting diodes. *Sci. Adv.* **2025**, *11*, eads7159.

[21] Zhan, L. L.; Li, S. X.; Li, Y. K.; Sun, R.; Min, J.; Bi, Z. Z.; Ma, W.; Chen, Z.; Zhou, G. Q.; Zhu, H. M. et al. Desired open-circuit voltage increase enables efficiencies approaching 19% in symmetric-asymmetric molecule ternary organic photovoltaics. *Joule* **2022**, *6*, 662–675.

[22] Jia, Y. H.; Li, R. C.; Zhou, Y.; Zhao, S. H.; Yu, H.; Wang, J. P.; Lin, Z. Y.; Su, H. B.; Zhao, N. Unveiling the complex evolution in mixed Br–Cl perovskite precursors for high-efficiency deep-blue light-emitting diodes. *Small Struct.* **2023**, *4*, 2200393.

[23] Zhang, S. W.; Ma, F. L.; Jiang, J. H.; Wang, Z. Y.; Kwok, R. T. K.; Qiu, Z. J.; Zhao, Z.; Lam, J. W. Y.; Tang, B. Z. Aggregative luminescence from $CsPbBr_3$ perovskite precursors. *Angew. Chem., Int. Ed.* **2024**, *63*, e202408586.

[24] Bi, L. Y.; Fu, Q.; Zeng, Z. X.; Wang, Y. F.; Lin, F. R.; Cheng, Y. H.; Yip, H. L.; Tsang, S. W.; Jen, A. K. Y. Deciphering the roles of MA-based volatile additives for α-$FAPbI_3$ to enable efficient inverted perovskite solar cells. *J. Am. Chem. Soc.* **2023**, *145*, 5920–5929.

[25] Feng, W. J.; Lin, K. B.; Li, W. Q.; Xiao, X. T.; Lu, J. X.; Yan, C. Z.; Liu, X. Y.; Xie, L. Q.; Tian, C. B.; Wu, D. et al. Efficient all-inorganic perovskite light-emitting diodes enabled by manipulating the crystal orientation. *J. Mater. Chem. A* **2021**, *9*, 11064–11072.

[26] Kühne, T. D.; Iannuzzi, M.; Del Ben, M.; Rybkin, V. V.; Seewald, P.; Stein, F.; Laino, T.; Khaliullin, R. Z.; Schütt, O.; Schiffmann, F. et al. CP2K: An electronic structure and molecular dynamics software package-quickstep: Efficient and accurate electronic structure calculations. *J. Chem. Phys.* **2020**, *152*, 194103.

[27] Martínez, L.; Andrade, R.; Birgin, E. G.; Martínez, J. M. PACKMOL: A package for building initial configurations for molecular dynamics simulations. *J. Comput. Chem.* **2009**, *30*, 2157–2164.

[28] Nosé, S. A unified formulation of the constant temperature molecular dynamics methods. *J. Chem. Phys.* **1984**, *81*, 511–519.

[29] VandeVondele, J.; Hutter, J. Gaussian basis sets for accurate calculations on molecular systems in gas and condensed phases. *J. Chem. Phys.* **2007**, *127*, 114105.

[30] Goedecker, S.; Teter, M.; Hutter, J. Separable dual-space Gaussian pseudopotentials. *Phys. Rev. B* **1996**, *54*, 1703–1710.